Research Square

Preprints are preliminary reports that have not undergone peer review.
They should not be considered conclusive, used to inform clinical practice,
or referenced by the media as validated information.

Development and demonstration of a Modular Astrobiological Experiments (MAEx) payload for autonomous biological monitoring in Low Earth Orbit (LEO)

Yamini Jangir

jangir@iitk.ac.in

Indian Institute of Technology Kanpur

Samrat Ghosh

Indian Institute of Technology Kanpur

Vinay Nayaka

Indian Institute of Technology Kanpur

Mubashir Ali

Indian Institute of Technology Kanpur

Dharshan Hegde

Indian Institute of Technology Kanpur

Kunal Mooley

Indian Institute of Technology Kanpur

Arunima Saha

Indian Institute of Technology Kanpur

Hariharan VC

Indian Institute of Technology Kanpur

Sujata Malik

Indian Institute of Technology Kanpur

Amey Bagare

Indian Institute of Technology Kanpur

Saurav Mishra

Indian Institute of Technology Kanpur

Mukuljeet Singh Mehrolia

Indian Institute of Technology Kanpur

Saravanan Matheswaran

Indian Institute of Technology Kanpur

Ashwani Kumar Thakur

Indian Institute of Technology Kanpur

Article

Keywords:

Posted Date: May 28th, 2026

DOI: https://doi.org/10.21203/rs.3.rs-9821917/v1

License: This work is licensed under a Creative Commons Attribution 4.0 International License.
Read Full License

Additional Declarations: No competing interests reported.

Abstract

The spaceflight environment presents unique physicochemical conditions, including microgravity, ionizing radiation, altered fluid transport, and confined habitats, that influence biological systems and biomolecular assembly processes. These conditions also create opportunities for space biomanufacturing and autonomous biofabrication by enabling low-resource, scalable biological production systems that may support long-duration human exploration. However, translating biological processes into operational space technologies requires compact, autonomous, and flight-compatible experimental platforms capable of functioning under constraints associated with orbital deployment, including limited volume, low power consumption, thermal regulation, and autonomous operation. Here, we present the Modular Astrobiology Experiment (MAEx) platform, a compact 3U spaceflight-compatible payload developed for autonomous multimodal biological characterization under space-relevant conditions. MAEx integrates imaging, absorption and fluorescence spectroscopy, and electrochemical sensing within a modular architecture, enabling simultaneous monitoring of microbial growth, extracellular electron transfer (EET), metabolic activity, and protein aggregation dynamics. To demonstrate platform versatility, the payload incorporates representative biological systems spanning cellular and molecular scales, including the electroactive bacterium *Shewanella oneidensis* MR-1, the radiation-resistant fungus *Ustilago maydis* FB1, and the human eye lens protein γD-crystallin. Ground-based characterization validated the functionality of the integrated analytical modules, including optical monitoring of microbial and biomolecular processes together with electrochemical interrogation using an in-house-developed potentiostat architecture. Collectively, MAEx establishes a scalable and adaptable framework for future space biology and biomanufacturing investigations relevant to bioregenerative life-support systems, in situ resource utilization, and autonomous biological production in space.

1. Introduction

Space imposes a range of physicochemical constraints on life, including altered gravity, ionizing radiation, and extreme temperature and pressure regimes, while spaceflight introduces additional engineered conditions such as microgravity and controlled atmospheres that shape biological responses[1–3]. For sustained human presence beyond Earth, it is therefore essential to evaluate the viability of biological systems across both contexts. Initiatives such as MELiSSA (Micro-Ecological Life Support System Alternative) demonstrate the feasibility of leveraging microbial processes for waste recycling, resource recovery, and atmospheric regeneration[4], providing a systems-level framework for closed-loop life support. Within this framework, life-support functions are distributed across interconnected compartments that collectively enable recycling of carbon, nitrogen, and water, including anaerobic degradation of waste, photoheterotrophic conversion of intermediates, nitrification, and photosynthetic production of oxygen and biomass coupled to higher plant systems. By emphasizing metabolic functionality and interdependence rather than individual taxa, this approach offers a blueprint for designing reduced yet resilient microbial consortia. Such systems, likely operating within engineered

enclosures on planetary surfaces, must be optimized for resource efficiency under space-relevant stressors, given the high cost of transporting raw materials and limited opportunities for replenishment[5].

Although terrestrial simulation platforms provide an important first step for investigating microbial responses to microgravity[6,7] and radiation[8–10], the design and deployment of spaceflight payloads remain essential for accurately capturing biological responses to the full spectrum of space stressors. Ground based analogs such as clinostats, rotating wall vessels, and random positioning machines attempt to average the gravity vector over time; however, they do not eliminate gravity itself and therefore cannot fully reproduce true microgravity conditions[11]. Residual accelerations, shear forces, and rotational artifacts introduced by these systems can alter fluid dynamics, mass transfer, and cell surface interactions in ways that are not representative of spaceflight. For example, the absence of buoyancy driven convection in microgravity fundamentally changes nutrient diffusion, waste accumulation, and boundary layer formation around cells, phenomena that are only partially approximated in terrestrial simulators. These limitations can lead to discrepancies in microbial growth, gene expression, biofilm formation, protein aggregation, and metabolic activity when compared to observations from orbital platforms[12]. In addition, terrestrial systems often fail to capture the combined effects of microgravity with other space relevant factors such as chronic low dose radiation and operational perturbations. Hence, spaceflight payloads provide a critical validation platform, enabling direct measurement of biological processes under spaceflight conditions and supporting the development of robust life support systems for long duration human missions.

We present, Modular Astrobiology Experiment (MAEx) platform, a spaceflight-compatible 3U payload (30 x 10 x 10 cm^3) designed to investigate microbial growth dynamics (via imaging and absorption spectroscopy), its metabolic activity (via fluorescence spectroscopy and electrochemical signature), and protein aggregation kinetics (via optical turbidity measurements), providing multiple lines of evidence for biological function through different levels of organization. The platform uniquely integrates optical, electrochemical, and molecular readouts within a compact, flight-compatible architecture, enabling simultaneous multi-modal interrogation of biological processes.The modular design supports flexibility in experimental configuration and organism selection, allowing targeted investigation of processes relevant to life support systems and astrobiological questions. The biological systems were selected to include representative microbial models including a facultative anaerobe, *Shewanella oneidensis* MR-1[13], and radiation resistant *Ustilago maydis* FB1[14], alongside a long-lived human lens protein, γD-crystallin[15,16], enabling investigation across cellular and molecular scales. Together, these systems capture metabolic activity, stress adaptation, and protein assembly dynamics under space-relevant conditions.

This work is guided by three central questions. First, what constitutes an optimal modular payload design that balances experimental flexibility with constraints on volume, power, and data acquisition inherent to spaceflight platforms. Second, how can ground-based calibration and validation protocols be structured to reliably predict and benchmark biological responses observed under true spaceflight

conditions within the designed payload. Third, which microbial systems and model biomolecules provide the most informative combination of metabolic functionality, stress resilience, macromolecular stability, and relevance to life-support processes in space. Addressing these questions enables the development of a robust experimental framework that links engineering design with biological function, ultimately informing the deployment of efficient, scalable, and flight-ready bioregenerative systems for long-duration human exploration.

2. MAEx Science Goals

A diverse set of model organisms have historically underpinned spaceflight biology[1], enabling mechanistic insights across scales, from molecular responses to whole organism physiology. Classical microbial models such as *Escherichia coli* and *Bacillus subtilis* have been probed for gene regulation, mutation rates, and stress tolerance under microgravity[17,18] and radiation[19–22]. Eukaryotic systems, including *Saccharomyces cerevisiae*[23–25] and *Arabidopsis thaliana*[26,27] have provided key insights into DNA repair, cell cycle control, and gravitropic responses. Multicellular models such as Caenorhabditis *elegans*[28–30] and *Drosophila melanogaster*[31–33] have enabled studies of development, muscle degeneration, and aging in space. Interspecies interactions are also being investigated for virulence levels under spaceflight conditions[34]. More recently, Axiom Mission 4 (Ax-4) expands this set of lineages by incorporating well-established and functionally relevant biological systems, including microalgae such as *Chlorella sorokiniana* (CS-I), *Parachlorella kessleri* (PK-I), and *Dysmorphococcus globosus* (DG-HI), which were proposed for their metabolic roles in waste recycling, life support integration, and oxygen production in space station environments[35,36]. In addition, the mission included a crop species, *Oryza sativa*[37], and extremophile, the tardigrade[38,39], to investigate biological resilience and functional capability under spaceflight conditions. Taken together, these organisms widen the list of organisms studied under spaceflight conditions.

Alongside cellular systems, protein aggregation and amyloid formation have also emerged as important targets of spaceflight and microgravity research as they are governed by diffusion, intermolecular interactions, and fluid transport processes that are significantly affected by gravity. Previous studies have investigated amyloid fibril formation of proteins including insulin, amyloid-β ($A\beta_{42}$), transthyretin, and α-synuclein under real or simulated microgravity conditions, demonstrating that microgravity can alter aggregation kinetics, fibril morphology, and intermolecular assembly pathways[40]. Amyloidogenesis via interfacial shear in a containerless biochemical reactor aboard the International Space Station (ISS)[41]. Spaceflight and ISS-based studies have additionally explored amyloid formation in relation to neurodegenerative diseases such as Alzheimer's and Parkinson's disease, where suppression of sedimentation and convection enables investigation of diffusion-limited aggregation processes that are difficult to isolate under terrestrial conditions[42]. These studies highlight the importance of microgravity as a unique platform for understanding protein aggregation mechanisms and motivate the inclusion of γD-crystallin aggregation measurements within the MAEx payload.

The design and validation of the Modular Astrobiology Experiment (MAEx) platform incorporates biological systems spanning bacterial, eukaryotic, and protein-based model systems to capture diverse aspects of biological function under space-relevant conditions. These systems were selected to investigate complementary processes including microbial metabolism, stress adaptation, and macromolecular assembly dynamics. Importantly, the modular architecture of the MAEx platform enables integration of a wide range of microbial species, protein biomolecules, and varied growth media, allowing the system to be readily adapted for different experimental objectives and astrobiological applications.

Shewanella oneidensis MR-1 is a facultative anaerobic, psychrotolerant bacterium capable of respiring a wide range of electron acceptors, including oxygen and insoluble metal oxides[43]. A defining feature of this organism is its ability to perform extracellular electron transfer (EET)[44], enabling reduction of minerals and interaction with solid-phase electron acceptors. This metabolic versatility underpins its relevance to bioelectrochemical systems, electromicrobial production, and biomining applications[45]. The capacity of *S. oneidensis* to couple metabolism with electron transfer makes it a suitable model for studying energy flux under space-relevant constraints. Previous studies have demonstrated its ability to reduce iron oxides in simulated Martian regolith (JSC-Mars1), resulting in significant iron mobilization[46], highlighting its potential role in *in situ resource utilization* (ISRU) strategies, including metal recovery and redox-driven processes in extraterrestrial environments. Investigating the growth physiology and electron transfer dynamics of *S. oneidensis* under spaceflight conditions is therefore relevant for sustainable space exploration..

Ustilago maydis is a eukaryotic fungal model organism widely used to study host-pathogen interactions and cellular stress responses. In addition to its role in plant pathology, this organism is capable of producing a range of secondary metabolites, including melanin and extracellular polysaccharides (EPS). Melanin production contributes to resistance against ultraviolet and ionizing radiation[14], making *U. maydis* a relevant model for studying stress tolerance in space environments. The organism possesses efficient DNA repair mechanisms, including homologs of genes involved in genome stability[47]. These characteristics position *U. maydis* as a model for investigating eukaryotic cellular adaptation, radiation resistance, and metabolite production under spaceflight conditions, with implications for both biotechnology and human health in space.

To complement biomolecular models, MAEx incorporates human γD-crystallin (HγD-Crys) as a model system to investigate protein stability and aggregation under microgravity. A human eye lens is composed of ~ 90% crystallin proteins, encompassing the α-, β-, and γ-crystallin families[48]. These proteins maintain high solubility throughout life to preserve lens transparency and refractive function, a process supported in part by the chaperone activity of α-crystallin[49]. The nuclear region cells of the lens are densely packed with crystallins and lack the capacity for protein synthesis or turnover, resulting in exceptionally long-lived proteins. This intrinsic constraint renders the lens nucleus particularly susceptible to cumulative post-translational modifications and oxidative stress, UV damage, ultimately

leading to crystallin destabilization, aggregation, and cataract formation[16,47]. Under destabilizing conditions, structural proteins like γD-crystallin undergoes protein misfolding and aggregation, producing light-scattering assemblies that can be monitored optically. Because protein aggregation is strongly influenced by diffusion, intermolecular interactions, and fluid transport, γD-crystallin provides a suitable model for studying aggregation dynamics under microgravity conditions. This aggregation of crystallins, in MAEx payload, will serve as a molecular model for examining protein misfolding and aggregation mechanisms under microgravity.

Collectively, these systems enable MAEx to bridge scales from cellular metabolism to molecular stability, providing an integrated framework to investigate how biological function and biomolecular integrity are shaped under spaceflight conditions. The current payload design operates as a sealed system maintained at approximately 1 atm pressure with integrated radiation shielding; however, the platform can be further modified to support anaerobic conditions and the cultivation of anaerobic lifeforms for future space biology investigations. These insights are expected to inform the design of robust biological systems for long-duration space missions and in situ resource utilization.

3. Payload Description

The MAEx payload is designed as a modular, multimodal bioanalytical system comprising six primary subsystems: a power distribution module, a control and data handling module, three biological analytical modules (imaging, spectroscopy, and electrochemistry), and a housekeeping module (Fig. 1). This architecture enables coordinated acquisition of biological and environmental data under spaceflight-relevant conditions.The detailed components of the payload are listed (Supplementary Table 1).

3.1 Payload Architecture and Mechanical Structure

The MAEx payload consists of a modular, mechanically integrated framework containing analytical modules, biochambers, thermal regulation components, power distribution electronics, and onboard computing systems centered around a Raspberry Pi 3 B+ (Fig. 2A). The payload was designed to satisfy spaceflight constraints associated with volume (3U; 10 × 10 × 30 cm), mass (~ 2.7 kg), thermal regulation (25–30°C), and power consumption (~ 6.5 W idle and < 20 W peak using a 24–36 V power bus), while maintaining compatibility with autonomous biological experimentation. The overall architecture comprises four primary subsystems: the analytical module, power distribution system, control and data handling system, and housekeeping module. Analytical operations are implemented in Python 3, with experimental data stored locally onboard and subsequently transmitted through the parent satellite communication system. The payload additionally incorporates regulated power distribution, periodic data logging, and timestamp synchronization through an onboard real-time clock (RTC) module.

The primary structural framework is fabricated from Al 6061 alloy, while the biological and electrochemical chambers are constructed from polycarbonate. Printed circuit boards (PCBs) are

manufactured using FR4 fiberglass-reinforced epoxy laminate due to its mechanical strength, electrical insulation, and flame-retardant properties. MAEx follows a fully modular, non-welded structural design in which all components are assembled using fasteners, spacers, and interlocking structural elements. The three experimental modules are vertically stacked using spacers for mechanical separation and subsystem protection, while electronic boards are mounted within a dedicated cage structure secured to the payload walls. These strategies provide structural rigidity, thermal isolation, and vibration tolerance during launch conditions. induced vibrations while also maintaining appropriate thermal and electrical isolation between subsystems.

The Raspberry Pi 3 B+ serves as the central processing and control unit for payload operation and was selected because of its compact form factor, low power consumption, computational flexibility, extensive peripheral interfacing capability, and compatibility with Python-based autonomous experiment control. Although microgravity itself is not expected to directly affect the operation of the Raspberry Pi, spaceflight deployment requires consideration of radiation-induced effects including transient bit flips, communication errors, and data corruption [50–52]. Previous radiation tolerance studies have demonstrated that Raspberry Pi Zero W boards can survive total ionizing doses approaching ~ 500 Gy(Si) under low-dose-rate ^{60}Co irradiation conditions[53], supporting the potential feasibility of COTS single-board computers for short-duration spaceflight applications, although mission-specific radiation validation remains essential. To improve robustness under low Earth orbit (LEO) conditions, MAEx incorporates localized aluminum shielding around sensitive electronics together with multilayer insulation (MLI) composed of aluminized Mylar and Kapton layers for thermal and environmental protection. Aluminum support plates additionally provide structural rigidity and thermal coupling for active temperature regulation. Collectively, the modular architecture enables scalable integration of future sensing systems while maintaining compatibility with compact small-satellite platforms.

3.2 Analytical Modules

The MAEx payload integrates three complementary analytical modules imaging, spectroscopy, and electrochemistry, to enable multimodal characterization of biological systems. These modules will capture spatial, optical, and functional signatures of microbial growth and molecular processes within a modular payload. Together, they will provide temporally resolved and cross-validated measurements across cellular and metabolic scales.

The imaging module employs a Raspberry Pi-based imaging system for time-resolved monitoring of microbial growth within the biochambers (Fig. 2B). Previous studies have demonstrated the utility of Raspberry Pi platforms for automated time-lapse imaging applications, including plant phenotyping and long-duration biological monitoring[54]. Other spaceflight-compatible imaging systems have utilized stabilized thermoelectrically cooled monochrome cameras, such as the Ascent A8050 (Apogee Imaging Systems, California, USA), for fluorescence imaging of *Arabidopsis* specimens under controlled conditions[55]. In MaEx, each culture well is positioned above an LED illumination array (XL-5050UWC, XINGLIGHT), while imaging is performed using a camera (Raspberry Pi Camera Module 3 Wide,

Raspberry Pi) mounted above the biochamber. Images are acquired at predefined intervals (0.5 hrs) and stored in PNG format with timestamp-based filenames. To minimize optical distortion and improve redundancy, two cameras with overlapping fields of view are deployed, each covering approximately two-thirds of the biochamber assembly. This configuration enables reliable visualization of microbial growth dynamics and spatial heterogeneity during long-duration experiments.

The spectroscopy module quantifies biological growth and biochemical changes by measuring optical transmission through liquid samples (Fig. 2B). Previous studies have demonstrated the development of compact LED-photodiode optical sensing systems for autonomous biological monitoring across terrestrial and spaceflight environments. Platforms such as MicrobeMeter[56], TubeOD[57], and ClampOD[57] employed low-cost LEDs, silicon photodiodes, and microcontroller-based electronics for continuous optical density measurements in microbial cultures, anaerobic systems, and thermophilic growth environments, while related Turbidimeter[58] adapted for blood culture monitoring using integrated 3D-printed optical assemblies. In spaceflight applications, missions including GeneSat-1[59], PharmaSat[60], O/OREOS[61], EcAMSat[62], BioSentinel[63], and LabSat[64] employed single or multiwavelength LED-photodiode optical systems for autonomous monitoring of microbial growth under orbital conditions. Among these, the BioSentinel platform additionally incorporated the metabolic indicator dye alamarBlue to quantify cellular metabolic activity during spaceflight experiments. More recently, the BioSentinel architecture has also been proposed for the long-duration Lunar Explorer Instrument for Space Biology Applications (LEIA) mission[65]. Building upon these earlier systems, the MAEx spectroscopy module expands the scope of autonomous optical biosensing by integrating parallel multiwell measurements with multimodal biological characterization capabilities relevant to both microbial physiology and biomolecular stability studies. In addition to monitoring microbial growth through optical density (OD_{600}), the system is designed to quantify fluorescence-associated signals associated with biomolecules (NADH) dynamics within a compact and modular payload architecture. Among endogenous fluorophores, reduced nicotinamide adenine dinucleotide (NADH) is widely recognized as a sensitive indicator of cellular metabolic activity because it directly participates in respiration and intracellular redox reactions[66–68]. NADH exhibits characteristic excitation and emission maxima near 340 nm and 460 nm, respectively, enabling non-invasive monitoring of microbial physiology and metabolic state. While absorbance measurements at 340 nm can quantify NADH concentration, fluorescence detection at 460 nm provides substantially higher sensitivity and specificity for detecting metabolically active cells, particularly in low-biomass or spaceflight-relevant environments. MAEx module incorporates ultraviolet (UV) LEDs (MT3650W3-UV by Marktech optoelectronics) and red LEDs (Generic) as light sources coupled with wavelength-specific UV and visible-range photodiodes for detection (UV photodiode : MICROFJ-30035-TSV-TR by Onsemi and optical photodiode : OPT101P by Texas Instruments). A custom 9-well biochamber, with each well (ca. 6 mL total volume; optical path length ca. 2.4 cm), is positioned between the light sources and photodetectors to enable simultaneous optical measurements across multiple samples. Transmitted light intensity from each well is converted into electrical signals by the corresponding photodiodes and digitized using an analog-to-digital converter (ADC; ADS1115 by Texas Instruments) interfaced with the Raspberry Pi through the I^2C communication protocol. Measurements

are stored as timestamped CSV files, enabling temporal analysis of optical density and fluorescence-associated signals related to microbial growth and protein aggregation dynamics.

The electrochemical module measures microbial metabolic activity through monitoring of EET using a three-electrode configuration (Fig. 2B). Only a few spaceflight studies have demonstrated the feasibility of employing electroactive microorganisms for bioelectrochemical applications under microgravity conditions. In 2019, the Micro-12 flight experiment conducted aboard the ISS investigated the effects of microgravity on the physiology of the model EET organism, *S. oneidensis* MR-1[69]. The study demonstrated enhanced insoluble ferrihydrite reduction in spaceflight compared to ground conditions. More recently, microbial fuel cell (MFC) experiments aboard the ISS demonstrated increased voltage and power generation by *S. oneidensis* biofilms under microgravity conditions[70]. While previous ISS microbial fuel cell experiments successfully demonstrated that *S. oneidensis* biofilms remain electrochemically active and capable of power generation under microgravity conditions, these systems primarily measured bulk electrical output and lacked the ability to precisely control electrode potentials or interrogate mechanistic EET processes. The MAEx electrochemical module expands upon these earlier studies through the implementation of a three-electrode potentiostat architecture capable of applying defined electrode potentials at the working electrodes to mimic mineral reduction environments encountered by electroactive microorganisms. A custom four-channel potentiostat was developed to enable parallel electrochemical measurements across four independent electrochemical biowells integrated within the biochamber assembly. The MAEx potentiostat architecture is a modified version of previous Arduino-based JUAMI potentiostat design[71] and redesigned around a Raspberry Pi-based control system to enable autonomous operation and seamless integration with the overall payload electronics. The system incorporates differential amplifier circuitry together with a 12-bit DAC (MCP4921) and 16-bit ADC (ADS1115) for improved analog signal generation and acquisition, enabling programmable electrochemical techniques such as cyclic voltammetry and chronoamperometry. A custom four-channel potentiostat was developed to support parallel electrochemical measurements across independent biowells. The 12-bit DAC replaced the PWM-based voltage generation used in the original JUAMI framework, providing more stable analog outputs, while the ADS1115 enabled high-resolution current acquisition through the Raspberry Pi platform. Integration of the potentiostat within the central Raspberry Pi architecture enabled unified hardware and software control across the entire MAEx payload.

3.3 Biochamber Design

The biochamber platform consists of a custom-designed polycarbonate (PC) device. The wells are directly machined into the central PC substrate, while an additional thin PC layer serves as the top cover to improve mechanical rigidity and structural stability during launch and microgravity operation (Fig. 2B). For spaceflight compatibility, the chamber is enclosed on both sides using optically transparent Zeonor layers bonded through precision-cut pressure-sensitive adhesive (PSA) interfaces. The PSA layers are aligned with the well geometry to provide reliable sealing while maintaining optical access to each culture chamber. The multilayer PC-PSA-Zeonor configuration minimizes leakage and evaporation while

enabling stable optical measurements during long-duration experiments. Zeonor was selected because of its high optical transparency, low autofluorescence, and lower water permeability relative to polycarbonate[63].

Two biochamber configurations were developed for integration with different analytical modules of the payload. The first configuration (Supplementary Fig. 1A) was optimized for the imaging and spectroscopy analytical modules and consists of a 3 × 3 array of culture wells, with each well accommodating approximately 6 mL of culture volume. The second configuration (Supplementary Fig. 1B), referred to as the electrochemical biochamber, was designed for integration with the electrochemical analytical module and consists of a 2 × 2 array of culture wells, each accommodating approximately 36 mL of culture volume.

The electrochemical biochamber incorporates a three-electrode sensing system consisting of a working electrode (WE), counter electrode (CE), and reference electrode (RE). This design was inspired by previous single-chamber three-electrode electrochemical reactor systems that successfully enriched subsurface electroactive microorganisms and were later proposed for microbial electrotechnology applications using defined microbial cultures [72–74], and have been suggested a putative design electrobiotechnology application from single species microbial culture[75]. In the present design, precision-machined openings in the PC top cover and Zeonor layer enable direct electrode insertion into individual culture wells. The working electrode consists of carbon cloth connected to a titanium wire, the counter electrode is composed of platinum mesh, and the reference electrode is a miniaturized Ag/AgCl electrode. Electrode interfaces are sealed within the multilayer assembly using compression-assisted bonding to maintain fluid containment and mechanical stability under spaceflight conditions. This configuration enables monitoring of microbial metabolism, EET, and redox activity while remaining compatible with the optical measurement architecture of the payload.

3.4 House-keeping Module

The housekeeping module monitors environmental parameters within the payload, including temperature and pressure, using distributed sensors placed at key locations. Temperature is regulated using a thermoelectric cooler, TEC (make, model) to maintain conditions within approximately 25–30°C. While temperature is continuously monitored for control purposes, discrete measurements are recorded at the start of each experimental cycle and stored alongside experimental data. Environmental data are integrated as metadata with imaging and spectroscopy outputs, ensuring traceability of experimental conditions.

3.5 Power Distribution System

Various voltage regulation techniques exist, including linear regulators, low-dropout regulators, and switching regulators. For this system, power conditioning will be achieved using switching DC-DC buck converters, selected for their high efficiency and suitability for large input-to-output voltage conversion with minimal heat dissipation. The system accepts an input voltage in the range of 24–36 V and

regulates it to stable output voltages of 12 V and 5 V. The 12 V rail supplies high-power components, including the potentiostat and LED arrays, while the 5 V rail powers the Raspberry Pi and associated electronics. Additional voltage requirements, such as the 25–30 V bias required for UV photodiodes, are provided through dedicated regulation circuits.

3.6 Control System and Data Handling

The control logic follows a cyclic execution scheme (Fig. 3A), with each cycle defined by a fixed duration of approximately 30 minutes. At the start of each cycle, a global timer is reset and flag variables (F2 and F3) are initialized to zero, indicating that the spectroscopy and electrochemical modules have not yet been executed within that iteration. The system first acquires housekeeping data, including temperature and pressure, which are recorded at the beginning of each cycle. Following this, the imaging module is executed, where LED illumination is activated, an image is captured, and illumination is subsequently turned off. The control flow then proceeds to the spectroscopy module, which is implemented through a nested loop. In this subroutine, photodiode measurements are acquired repeatedly (n = 10) to improve measurement precision and enable estimation of mean and variance. A counter variable (C), initialized at the start of the subroutine, is incremented with each iteration until the specified number of measurements is reached. Once spectroscopy measurements are completed, the electrochemical module is executed, wherein experimental parameters are set and current and voltage data are recorded using the potentiostat. After each module execution, the system checks whether the 30-minute cycle duration has elapsed. If time remains within the cycle, the system proceeds to the next pending experiment based on flag status; if all experiments are completed, the system remains idle until the cycle duration is reached. Upon completion of the cycle, the timer is reset and the sequence is repeated.

In parallel with the main control loop, an independent temperature regulation subroutine operates continuously (Fig. 3B). This routine receives temperature input from the main program and maintains thermal conditions within a predefined range (25–30°C) using a thermoelectric cooler (TEC). Heating or cooling is activated when the temperature falls outside this range. While temperature is continuously monitored for control purposes, only the discrete measurements acquired at the start of each cycle are stored as part of the experimental dataset.

All data generated by the biological measurement modules and housekeeping sensors are stored locally on the Raspberry Pi in structured formats (e.g., PNG for imaging data and CSV for sensor outputs). These data are periodically transmitted to the parent satellite platform for downlink to ground stations, ensuring reliable data retrieval and post-mission analysis.

3.7 Spaceflight Environmental Validation

The MAEx payload was designed to withstand the thermal, pressure, and operational constraints associated with deployment in low Earth orbit (LEO). Space environments expose payload systems to extreme temperature variations ranging from approximately − 160°C during eclipse conditions to over + 120°C under direct solar illumination, in addition to near-vacuum pressures of ~ 10^{-3}–10^{-5} hPa. To ensure reliable operation under these conditions, the payload incorporates both passive and active

thermal management strategies, including thermally conductive aluminum support structures, insulation layers, thermoelectric temperature regulation systems, and Kapton-film heaters. Structural sealing and multilayer chamber assembly were implemented to preserve chamber integrity and minimize leakage under low-pressure conditions. Materials used throughout the payload architecture were selected based on low thermal expansion, mechanical stability, compatibility with repeated thermal cycling, and low-outgassing characteristics to reduce risks of structural deformation and contamination of optical and electronic components during prolonged vacuum exposure.

Rapid orbital heating and cooling cycles can induce thermal expansion and contraction of structural components, potentially affecting sensor alignment and analytical measurements. Accordingly, the mechanical and optical subsystems were designed with thermal compensation considerations to maintain alignment stability during long-duration operation. Power distribution and battery subsystems were additionally designed to support sustained thermal regulation and autonomous payload functionality under fluctuating environmental conditions. Critical onboard electronics, including controllers, sensors, and communication interfaces, were selected based on tolerance to spaceflight-relevant environmental stresses, while autonomous control and subsystem-level redundancy were incorporated to improve overall payload survivability and mission reliability.

To ensure structural integrity and avoid resonance-induced failures during launch and operation, modal analysis was performed to evaluate the dynamic response of the MAEx payload. Determination of the natural frequencies and mode shapes is essential for assessing the vibration tolerance of spaceflight structures, particularly to avoid dynamic coupling with the host spacecraft. For the present mission profile, the natural frequency range of the mother spacecraft is estimated to lie between 70–90 Hz. Finite element modal simulations of the MAEx structure identified the first and most dominant mode at 218.72 Hz (Fig. 4). The dominant mode was determined based on the highest effective mass and participation factor values, both corresponding to the first mode shape. Since the primary natural frequency of the MAEx payload is substantially higher than that of the host spacecraft, the payload is expected to remain outside the resonance regime under nominal launch conditions. These results indicate favorable structural robustness of the payload architecture, although additional qualification studies, including random vibration and shock analyses, will be required prior to flight certification.

To evaluate the operational survivability of the MAEx payload under LEO thermal conditions, preliminary thermal simulations were conducted to estimate the temperature range expected during orbital operation. Understanding the thermal environment is critical for ensuring reliable performance of the biological experiments, electronic subsystems, and structural materials during repeated orbital heating and cooling cycles. Initial thermal assessment of the host platform was carried out using the Systems Tool Kit (STK; version 12; Ansys. Inc.) Space Environment and Effects Tool (SEET). Thermal and Vehicle Temperature Model, considering the ISRO POEM-4 platform operating in LEO. The simulations incorporated three primary external heat sources: direct solar radiation, Earth-reflected solar radiation (albedo), and infrared radiation emitted by the Earth. During sunlit orbital phases, all three heat sources contribute to the thermal balance, whereas during eclipse phases terrestrial infrared radiation becomes

the dominant contributor. The simulations predicted a temperature range between approximately − 80°C and − 10°C over a complete orbital cycle. These preliminary analyses provide an initial assessment of the thermal constraints relevant to payload operation and will guide future subsystem-level thermal qualification studies.

4. Biological Systems and Ground-based Functional Validation

To establish the scientific relevance of the MAEx payload for future spaceflight investigations, representative biological systems spanning microbial physiology, electroactive metabolism, and biomolecular stability were evaluated under controlled laboratory conditions. These systems were selected to probe biological processes directly relevant to long-duration space habitation and orbital biotechnology, including microbial growth, EET, stress adaptation, and protein aggregation dynamics. Ground-based experiments were performed using a combination of MAEx-compatible analytical workflows and complementary laboratory instrumentation to establish baseline biological responses prior to flight deployment. Together, these studies provide a framework for interpreting future spaceflight measurements and demonstrate the suitability of the selected model systems for autonomous multimodal monitoring under space-relevant conditions.

4.1 Multimodal Monitoring of Microbial Growth Kinetics

Microbial growth and activity were monitored across complementary measurement modalities to evaluate the performance of the MAEx payload under laboratory conditions. Both *Shewanella* and *Ustilago* were cultivated in YPD medium at 25 ^{O}C, enabling quantitative investigations of growth dynamics by employing optical, biochemical, and electrochemical signatures associated with cellular proliferation and metabolism.

Time-resolved imaging and spectroscopic measurements were used to monitor microbial growth dynamics within the biochambers. Imaging enabled direct visualization of growth, with both organisms showing a progressive increase in cell density over time, reflected by reduced transparency in the captured images (Supplementary Video 1). Two quantitative image-derived metrics, mean intensity and entropy, were used for analysis. Mean intensity was calculated as the average grayscale brightness of pixels within each detected well region, whereas entropy was calculated from the variability in grayscale pixel intensities within the same region (see Supplementary Methods). Quantitative analysis based on image mean intensity yielded peak doubling times of 12.6 h for *Shewanella* and 32.9 h for *Ustilago* (Fig. 5). A fisheye distortion effect was observed in the imaging data; consequently, two Raspberry Pi cameras were incorporated into the payload design to improve image coverage and reduce optical distortion.

Complementary spectroscopic measurements of *Shewanella* and *Ustilago* (Fig. 6A,B) yielded doubling times of 8.9 h and 10.3 h, respectively. Spectroscopy-based measurements for *Shewanella* showed trends broadly consistent with the image-based analysis, whereas the comparatively faster apparent

growth dynamics observed for *Ustilago* may reflect differences in how filamentous or surface-associated fungal growth influences optical density and image-derived intensity measurements. Previous studies have reported doubling times of approximately 2–4 h for *Shewanella* grown in rich LB medium[76] and approximately 2–3 h for *Ustilago* cultured in YPD medium under optimal aerobic conditions[77]. The comparatively longer apparent doubling times observed in the present study likely arise from static incubation conditions, growth on semi-solid agar within confined well geometries, and differences in nutrient availability and growth temperature relative to standard laboratory culture conditions.

Optical density (OD_{600}) measurements alone provide limited information regarding the physiological or metabolic state of the culture at a given timepoint, particularly once cell density stabilizes. Therefore, fluorescence measurements (Ex/Em: 365/460 nm) targeting intrinsic NADH autofluorescence were employed as an additional proxy for cellular metabolic activity and redox state[67]. The emission profile showed a pronounced increase during exponential growth, peaking around day 3, followed by a definitive decrease. The initial rise reflects increased intracellular NADH levels associated with active metabolism and cell proliferation. The subsequent decline in fluorescence is indicative of reduced metabolic activity and a loss of actively growing cells as cultures transition into the stationary phase. Across both measurements, *Ustilago* exhibited higher signal intensity relative to *Shewanella*, likely reflecting differences in growth kinetics and metabolic activity associated with medium preference. YPD was selected as a common growth medium for both organisms, as *Ustilago* did not exhibit appreciable growth in LB over ~ 7 days (data not shown). Despite these differences in growth behavior, imaging and spectroscopy provided consistent and complementary readouts of microbial proliferation and physiological state across both organisms.

To evaluate whether a measurable electrochemical signature could be detected under initial payload conditions (oxic, 1 atm), the response of *Shewanella* was investigated using a single-chamber, three-electrode bioelectrochemical reactor supplemented with sediment slurry (Fig. 7). The biotic system exhibited a characteristic temporal evolution in current density, beginning with an initial decrease followed by a gradual increase after ca. 15–20 h. A pronounced rise in current was observed beyond ca. 40 h, reaching ca. 1.2–1.3 A/m^2 by ca. 90 h of incubation. In contrast, the abiotic control showed a steady decline in current density over time, stabilizing at ~ 0.12–0.15 A/m^2, indicating the absence of sustained electrochemical activity in the absence of microbes. The divergence between biotic and abiotic signals highlights the contribution of microbial processes to current generation. The delayed yet sustained increase in current in the biotic condition is consistent with the establishment of EET pathways and biofilm development on the electrode surface, under oxic conditions. These electrochemical trends align with growth progression observed via imaging and spectroscopy, supporting the use of *Shewanella* as a model system for probing metabolically driven electron transfer under conditions relevant to the MAEx payload.

4.2 Protein Aggregation Kinetics

To assess whether the MAEx spectroscopy module can reliably capture protein aggregation kinetics under controlled conditions, we monitored the aggregation behavior of γD-crystallin by measuring absorbance at 340 nm (Fig. 6C). A characteristic sigmoidal increase was observed over time, indicating progressive protein aggregation. The aggregation profile exhibited an initial lag phase followed by a rapid growth phase between ca. 10–20 days, and a subsequent plateau beyond ca. 30 days, consistent with saturation of aggregate formation. In contrast, the control sample remained stable with negligible change in optical density throughout the experiment, confirming that the observed signal increase was specific to γD-crystallin aggregation. The sigmoidal kinetics are indicative of a nucleation-dependent aggregation process, where initial formation of aggregation nuclei is followed by rapid growth and eventual equilibrium. These results demonstrate that γD-crystallin exhibits characteristic aggregation kinetics under the tested conditions, supporting its suitability as a model system for investigating protein aggregation under spaceflight-relevant conditions. Previous spaceflight payloads have also demonstrated the feasibility of autonomous optical biosensing for protein analysis in orbit. For example, the Tianzhou-1 cargo spacecraft carried an integrated payload for visual protein detection using immunoassay-based enrichment and CCD camera monitoring, highlighting the growing implementation of compact autonomous biomolecular sensing systems for spaceflight applications[78]. Microgravity investigations, onboard the ISS, have also investigated the transport and incorporation of fluorescent protein aggregates during protein crystal growth, demonstrating that microgravity influences aggregate behavior and biomolecular assembly dynamics[79]. Together with earlier protein crystallization studies conducted on ISS platforms, these investigations highlight the growing interest in understanding protein stability and self-assembly processes in spaceflight environments.

5. Functional Calibration of MAeX Analytical Modules

5.1 Imaging Module

To evaluate the imaging performance of the Raspberry Pi Camera Module 3 Wide, we characterized the field of view and image clarity as a function of working distance. The camera was mounted perpendicular to a calibrated grid, and images were acquired over distances ranging from 30 to 150 mm in increments of 10 mm. Initial experiments explored different lens adjustment settings; however, the final imaging workflow employed the camera’s autofocus mode, as fixed manual lens positions resulted in reduced image quality under low-light conditions arising during microbial growth. Therefore, lens adjustment values were not used as fixed operating parameters in the final payload configuration.Based on the field-of-view characterization, an optimal working distance range of 60–100 mm was identified (Supplementary Fig. 2), providing a suitable balance between image coverage and focus stability. These measurements informed the final configuration of the imaging module used in the MAEx payload.

5.2 Spectroscopic Module

To enable absorbance and fluorescence measurements, the spectroscopy module employs red (630 nm) and ultraviolet (365 nm) LEDs together with wavelength-specific photodiodes. Prior to payload

integration, the optical components were characterized to evaluate spectral performance, output stability, and temperature sensitivity under laboratory conditions (Figs. 8 and 9; Supplementary Figs. 3 and 4). The measured emission spectra closely matched manufacturer specifications and confirmed suitability for optical density and fluorescence measurements.

The integrated red LED-photodiode system was further calibrated to assess the influence of LED input voltage (V_{in}) and temperature on detector output voltage (V_{out}). Because the LEDs were powered directly through Raspberry Pi GPIO pins (~ 3.3 V), potential voltage fluctuations were evaluated with and without an LED driver circuit. Vin exhibited only minor variation (< 0.4%) and weak temperature dependence, whereas V_{out} showed a significantly stronger temperature dependence (Fig. 8B,C), indicating that detector response was dominated primarily by thermal effects rather than electrical instability. Also, introducing the LED driver does not affect the relative distribution of V_{out}, rather it substantially decreases signal amplitude and overall sensitivity. Consequently, subsequent biological experiments were performed without the LED driver, with temperature-based calibration applied to correct systematic detector variation. Similar calibration experiments performed using the UV photodiode system demonstrated minimal contribution of GPIO voltage fluctuations (~ 0.11%) relative to intrinsic and temperature-dependent detector variability (Fig. 9). To isolate intrinsic signal fluctuations from thermal effects, measurements were grouped into narrow temperature bins within which strong temperature dependence is not expected and they show significant variability (~ 5%) (Supplementary Fig. 4). Collectively, these results establish temperature as the primary source of signal variation for the red LED-photodiode system; whereas the UV photodiode system is dominated by intrinsic fluctuation. This provides the calibration framework necessary for accurate interpretation of absorbance and fluorescence measurements during biological experiments.

As an initial validation of the UV spectroscopy module, absorption coefficients at 365 nm were measured after 50 h of protein aggregation for γD-crystallin and control (DI water) samples.The measured absorption coefficients were $0.0134 \pm 0.0006\ mm^{-1}$ of water and $0.0164 \pm 0.0002\ mm^{-1}$ for γD-crystallin. Although these preliminary measurements demonstrate the capability of the integrated UV spectroscopy system to resolve differences in optical absorption, additional biological and technical replicates will be required to establish statistical significance and reproducibility.

5.3 Electrochemical Module

The performance of the single-channel potentiostat was evaluated using cyclic voltammetry (CV) measurements performed with a standard ferri/ferrocyanide redox system consisting of 10 mM potassium ferricyanide in 1 M KNO_3 supporting electrolyte (Fig. 10). The recorded cyclic voltammograms exhibited characteristic redox responses associated with the $Fe(CN)_6^{3-}/Fe(CN)_6^{4-}$ couple with a midpoint potential ($E_{1/2}$) of ca. 0.28 V vs. Ag/AgCl. This value is consistent with previously

reported midpoint potentials,usually varying due to electrolyte composition, ionic strength, electrode material, and uncompensated resistance effects[80–83].

The cyclic voltammetry characterization additionally verified the functionality of the transimpedance amplifier-based current sensing architecture, analog-to-digital acquisition electronics, and PWM-derived voltage control subsystem implemented within the electrochemical module. Minor fluctuations and noise observed (Fig. 10C) in the voltammograms are likely attributable to breadboard-level prototyping, electrode surface heterogeneity, uncompensated solution resistance, and PWM-derived voltage ripple. Nevertheless, the system reproducibly captured the characteristic electrochemical behavior of the $Fe(CN)_6^{3-}$/$Fe(CN)_6^{4-}$ redox couple, demonstrating the suitability of the custom potentiostat architecture for autonomous electrochemical measurements including chronoamperometry and cyclic voltammetry relevant to microbial EET studies.

6. Conclusion

Biological payloads flown aboard spaceflight platforms have historically focused on monitoring microbial survival[84–88]and gene expression[89,90] under microgravity and radiation exposure. While previous systems have demonstrated microbial cultivation, imaging, and environmental monitoring in orbit, many rely on a single analytical modality, limiting the ability to capture complementary physiological signatures in real time. Recent efforts have expanded CubeSat bioanalytical capabilities by integrating electrochemical ion-selective sensors with optical absorbance sensing for monitoring pH, sodium ion concentration, and absorbance changes in microorganisms growing within fluidic wells[91]. These studies established an important framework for incorporating multimodal sensing, fluidic systems, and onboard autonomous control into compact spaceflight-compatible payloads.

In this study, we present the design, development, and ground-based characterization of the MAEx payload, a modular multimodal bioanalytical platform for autonomous biological experimentation under spaceflight conditions. MAEx integrates imaging, spectroscopy, and electrochemical sensing within a compact small-satellite-compatible architecture. In contrast to ion-selective electrochemical sensing approaches primarily focused on environmental monitoring90, the MAEx electrochemical module employs an in-house-developed programmable three-electrode potentiostat designed to investigate microbial redox activity and EET processes using techniques such as cyclic voltammetry and chronoamperometry. Ground characterization experiments demonstrated the functionality of the individual analytical modules, including optical monitoring of microbial and biomolecular processes together with electrochemical interrogation using the custom potentiostat system. Collectively, MAEx establishes a scalable and adaptable framework for integrating multimodal biosensing with autonomous experimental control for future astrobiology, space biology, and bioelectrochemical investigations.

More broadly, this work addresses three key challenges relevant to next-generation biological payloads for spaceflight: development of modular payload architectures compatible with spacecraft constraints, establishment of ground-based validation frameworks for predicting biological performance under

spaceflight conditions, and identification of microbial and biomolecular systems relevant to stress resilience, redox metabolism, and bioregenerative life-support applications. Although the present study represents a ground-validated TRL-4 demonstration, MAEx provides a scalable experimental framework for future in-orbit investigations linking engineering design with biological function. Such integrated platforms will be essential for developing robust, autonomous, and flight-ready bioregenerative systems for long-duration human exploration beyond Earth orbit.

Declarations

Contributions:

SG contributed to payload development, performed spectroscopy and imaging module characterization, conducted biological experiments, and contributed to data acquisition and analysis. VN designed and characterized the imaging and electrochemical modules and potentiostat circuitry and contributed to electrochemical experiments and data analysis. MA contributed to payload design, integration, and thermal validation. DH assisted with biochamber and payload design. SM (Saurav Mishra) contributed to image analysis. AB performed and analyzed electrochemical proof-of-concept experiments. SM (Sujata Malik) performed protein aggregation proof-of-concept experiments. HVC performed the initial fungal growth experiments, and SM (Saravaranan Matheswaran) provided the fungal isolate used in the study. MS supervised the electrochemical design of the potentiostat. KM supervised the overall project and contributed to payload conceptualization and mission strategy. YJ conceived and supervised the overall project, coordinated biological experiments, and wrote the original manuscript. The manuscript was edited and reviewed by YJ, SG, VN, MA, MS, KM, and AKT. All authors reviewed and approved the final manuscript.

Acknowledgments:

AKT sincerely thanks Martin Zanni (Department of Chemistry, University of Wisconsin-Madison, USA) for providing the plasmid containing the γD-crystallin gene, which enabled overexpression of the γD-crystallin protein. KPM also acknowledges financial support from IIT Kanpur under project grants IITK/BSBE/20100293 and IITK/SPASE/2023222. AS sincerely thanks Mouchandra Paul for assistance with the initial use of the microbiology laboratory facilities (Advanced Imaging Center, IIT Kanpur). AS also thanks Gouri S. Nair for providing initial microbiological training. AS is also grateful to Kavikumar A. K. for assistance with the initial usage of the spectrofluorometer facility (S. Ganesh, IIT Kanpur). KPM and YJ are grateful to Aloke Kumar for initial discussions.

Ethics declarations:

The authors declare no competing interests.

References

1. Prasad, B. *et al.* How the space environment influences organisms: an astrobiological perspective and review. *Int. J. Astrobiol.* 20, 159–177 (2021).
2. Lu, Y., Shao, Q., Yue, H. & Yang, F. A Review of the Space Environment Effects on Spacecraft in Different Orbits. *IEEE Access* 7, 93473–93488 (2019).
3. Thirsk, R., Kuipers, A., Mukai, C. & Williams, D. The space-flight environment: the International Space Station and beyond. *CMAJ* 180, 1216–1220 (2009).
4. Poughon, L., Farges, B., Dussap, C. G., Godia, F. & Lasseur, C. Simulation of the MELiSSA closed loop system as a tool to define its integration strategy. *Adv. Space Res.* 44, 1392–1403 (2009).
5. Koehle, A. P., Brumwell, S. L., Seto, E. P., Lynch, A. M. & Urbaniak, C. Microbial applications for sustainable space exploration beyond low Earth orbit. *Npj Microgravity* 9, 1–27 (2023).
6. Zhang, Y. et al. NASA's Ground-Based Microgravity Simulation FacilityMicrogravity simulation facility. in Plant Gravitropism: Methods and Protocols (ed. Blancaflor, E. B.) 281–299 (Springer US, New York, NY, 2022). doi:10.1007/978-1-0716-1677-2_18.
7. Brungs, S. *et al.* Facilities for Simulation of Microgravity in the ESA Ground-Based Facility Programme. *Microgravity Sci. Technol.* 28, 191–203 (2016).
8. Simonsen, L. C., Slaba, T. C., Guida, P. & Rusek, A. NASA's first ground-based Galactic Cosmic Ray Simulator: Enabling a new era in space radiobiology research. *PLOS Biol.* 18, e3000669 (2020).
9. Norbury, J. W. *et al.* Galactic cosmic ray simulation at the NASA Space Radiation Laboratory. *Life Sci. Space Res.* 8, 38–51 (2016).
10. La Tessa, C., Sivertz, M., Chiang, I.-H., Lowenstein, D. & Rusek, A. Overview of the NASA space radiation laboratory. *Life Sci. Space Res.* 11, 18–23 (2016).
11. Ferranti, F., Del Bianco, M. & Pacelli, C. Advantages and Limitations of Current Microgravity Platforms for Space Biology Research. *Appl. Sci.* 11, 68 (2021).
12. Acres, J. M., Youngapelian, M. J. & Nadeau, J. The influence of spaceflight and simulated microgravity on bacterial motility and chemotaxis. *Npj Microgravity* 7, 1–11 (2021).
13. Ikeda, S. *et al.* Shewanella oneidensis MR-1 as a bacterial platform for electro-biotechnology. *Essays Biochem.* 65, 355–364 (2021).
14. Holloman, W. K., Schirawski, J. & Holliday, R. Towards understanding the extreme radiation resistance of Ustilago maydis. *Trends Microbiol.* 15, 525–529 (2007).
15. Mills, I. A., Flaugh, S. L., Kosinski-Collins, M. S. & King, J. A. Folding and stability of the isolated Greek key domains of the long-lived human lens proteins γD-crystallin and γS-crystallin. *Protein Sci.* 16, 2427–2444 (2007).
16. Kosinski-Collins, M. S. & King, J. In vitro unfolding, refolding, and polymerization of human γD crystallin, a protein involved in cataract formation. *Protein Sci.* 12, 480–490 (2003).
17. Aunins, T. R. *et al.* Spaceflight Modifies Escherichia coli Gene Expression in Response to Antibiotic Exposure and Reveals Role of Oxidative Stress Response. *Front. Microbiol.* 9, (2018).

18. Morrison, M. D., Fajardo-Cavazos, P. & Nicholson, W. L. Comparison of Bacillus subtilis transcriptome profiles from two separate missions to the International Space Station. *Npj Microgravity* 5, 1 (2019).
19. Horneck, G. Responses ofBacillus subtilis spores to space environment: Results from experiments in space. *Orig. Life Evol. Biosph.* 23, 37–52 (1993).
20. Vaishampayan, P. A., Rabbow, E., Horneck, G. & Venkateswaran, K. J. Survival of Bacillus pumilus Spores for a Prolonged Period of Time in Real Space Conditions. *Astrobiology* 12, 487–497 (2012).
21. Saffary, R. *et al.* Microbial survival of space vacuum and extreme ultraviolet irradiation: strain isolation and analysis during a rocket flight. *FEMS Microbiol. Lett.* 215, 163–168 (2002).
22. Takahashi, A. *et al.* Mutation Frequency of Plasmid DNA and Escherichia coli Following Long-term Space Flight on Mir. *J. Radiat. Res. (Tokyo)* 43, S137–S140 (2002).
23. Stahl-Rommel, S. *et al.* A CRISPR-based assay for the study of eukaryotic DNA repair onboard the International Space Station. *PLOS ONE* 16, e0253403 (2021).
24. Nislow, C. *et al.* Genes Required for Survival in Microgravity Revealed by Genome-Wide Yeast Deletion Collections Cultured during Spaceflight. *BioMed Res. Int.* 2015, 976458 (2015).
25. Mizukami-Murata, S. *et al.* Genome-Wide Expression Changes in Saccharomyces cerevisiae in Response to High-LET Ionizing Radiation. *Appl. Biochem. Biotechnol.* 162, 855–870 (2010).
26. Olanrewaju, G. O. *et al.* Integrative transcriptomics and proteomics profiling of Arabidopsis thaliana elucidates novel mechanisms underlying spaceflight adaptation. *Front. Plant Sci.* 14, (2023).
27. Land, E. S., Sheppard, J., Doherty, C. J. & Perera, I. Y. Conserved plant transcriptional responses to microgravity from two consecutive spaceflight experiments. *Front. Plant Sci.* 14, (2024).
28. Scott, A. *et al.* Caenorhabditis elegans in microgravity: An omics perspective. *iScience* 26, (2023).
29. Honda, Y., Honda, S., Narici, M. & Szewczyk, N. J. Spaceflight and Ageing: Reflecting on Caenorhabditis elegans in Space. *Gerontology* 60, 138–142 (2013).
30. Selch, F. *et al.* Genomic response of the nematode *Caenorhabditis elegans* to spaceflight. *Adv. Space Res.* 41, 807–815 (2008).
31. Marcu, O. *et al.* Innate Immune Responses of Drosophila melanogaster Are Altered by Spaceflight. *PLOS ONE* 6, e15361 (2011).
32. Ma, L., Ma, J. & Xu, K. Effect of Spaceflight on the Circadian Rhythm, Lifespan and Gene Expression of Drosophila melanogaster. *PLOS ONE* 10, e0121600 (2015).
33. Ogneva, I. V., Belyakin, S. N. & Sarantseva, S. V. The Development Of Drosophila Melanogaster under Different Duration Space Flight and Subsequent Adaptation to Earth Gravity. *PLOS ONE* 11, e0166885 (2016).
34. Gilbert, R. *et al.* Spaceflight and simulated microgravity conditions increase virulence of Serratia marcescens in the Drosophila melanogaster infection model. *Npj Microgravity* 6, 4 (2020).
35. Matula, E. E. & Nabity, D. J. A. Metabolic response of *Chlorella vulgaris* to a transient thermal environment for supporting simultaneous air revitalization and thermal control in a crewed habitat.

Acta Astronaut. 187, 406–415 (2021).

36. Revellame, E. D. *et al.* Microalgae cultivation for space exploration: Assessing the potential for a new generation of waste to human life-support system for long duration space travel and planetary human habitation. *Algal Res.* 55, 102258 (2021).
37. Jin, J., Chen, H. & Cai, W. Transcriptome Analysis of Oryza sativa Calli Under Microgravity. *Microgravity Sci. Technol.* 27, 437–453 (2015).
38. Rizzo, A. M. *et al.* Space Flight Effects on Antioxidant Molecules in Dry Tardigrades: The TARDIKISS Experiment. *BioMed Res. Int.* 2015, 167642 (2015).
39. Weronika, E. & Łukasz, K. Tardigrades in Space Research - Past and Future. *Orig. Life Evol. Biospheres* 47, 545–553 (2017).
40. Matsushita, H. *et al.* Amyloid fibril formation is suppressed in microgravity. *Biochem. Biophys. Rep.* 25, 100875 (2021).
41. McMackin, P., Adam, J., Griffin, S. & Hirsa, A. Amyloidogenesis via interfacial shear in a containerless biochemical reactor aboard the International Space Station. *Npj Microgravity* 8, 41 (2022).
42. Zhou, J. *et al.* Effects of sedimentation, microgravity, hydrodynamic mixing and air–water interface on α-synuclein amyloid formation. *Chem. Sci.* 11, 3687–3693 (2020).
43. Bretschger, O. *et al.* Current production and metal oxide reduction by Shewanella oneidensis MR-1 wild type and mutants. *Appl. Environ. Microbiol.* 73, 7003–7012 (2007).
44. Shi, L. *et al.* Extracellular electron transfer mechanisms between microorganisms and minerals. *Nat. Rev. Microbiol.* 14, 651–662 (2016).
45. Kim, B. *et al.* Progress and Prospects for Applications of Extracellular Electron Transport Mechanism in Environmental Biotechnology. *ACS EST Eng.* 4, 1520–1539 (2024).
46. Castelein, S. M. *et al.* Iron can be microbially extracted from Lunar and Martian regolith simulants and 3D printed into tough structural materials. *PLOS ONE* 16, e0249962 (2021).
47. Holliday, R. Early studies on recombination and DNA repair in *Ustilago maydis*. *DNA Repair* 3, 671–682 (2004).
48. Acosta-Sampson, L. & King, J. Partially Folded Aggregation Intermediates of Human γD-, γC-, and γS-Crystallin Are Recognized and Bound by Human αB-Crystallin Chaperone. *J. Mol. Biol.* 401, 134–152 (2010).
49. Feng, J., Smith, D. L. & Smith, J. B. Human Lens β-Crystallin Solubility*. *J. Biol. Chem.* 275, 11585–11590 (2000).
50. Guertin, S. Raspberry Pis for Space Guideline. NASA WBS 7242974049 http://nepp.nasa.gov/.
51. Mojica Decena, J., Wood, B., Martineau, R., Dennison, J. R. & Tayor, M. Radiation Damage Threshold of Satellite COTS Components: Raspberry Pi Zero for OPAL CubeSat. Stud. Res. Symp. https://digitalcommons.usu.edu/mp_post/67 (2018).
52. Violette, D. P. Arduino-Raspberry Pi: Hobbyist Hardware and Radiation Total Dose Degradation. (2014).

53. Hanson, S. C. & Hayes, R. B. Radiation Hardness Assurance by Redundancy in Raspberry Pi Zero W Computation Metrics via Total Ionizing Dose 60Co Testing for Spacecraft Applications. *Health Phys.* 128, 457 (2025).
54. Tovar, J. C. *et al.* Raspberry Pi–powered imaging for plant phenotyping. *Appl. Plant Sci.* 6, e1031 (2018).
55. Bamsey, M. T., Paul, A.-L., Graham, T. & Ferl, R. J. Flexible imaging payload for real-time fluorescent biological imaging in parabolic, suborbital and space analog environments. *Life Sci. Space Res.* 3, 32–44 (2014).
56. Sasidharan, K., Martinez-Vernon, A. S., Chen, J., Fu, T. & Soyer, O. S. A low-cost DIY device for high resolution, continuous measurement of microbial growth dynamics. Preprint at https://doi.org/10.1101/407742 (2018).
57. Deutzmann, J. S. *et al.* Low-Cost Clamp-On Photometers (ClampOD) and Tube Photometers (TubeOD) for Online Cell Density Determination. *Front. Microbiol.* 12, (2022).
58. Barbé, B. *et al.* Pilot Testing of the “Turbidimeter”, a Simple, Universal Reader Intended to Complement and Enhance Bacterial Growth Detection in Manual Blood Culture Systems in Low-Resource Settings. *Diagnostics* 12, (2022).
59. Kitts, C. et al. Flight Results from the GeneSat-1 Biological Microsatellite Mission. Proc. 21st Annu. AIAAUSU Conf. Small Satell. https://digitalcommons.usu.edu/smallsat/2007/all2007/69 (2007).
60. Ricco, A. J. et al. PharmaSat: drug dose response in microgravity from a free-flying integrated biofluidic/optical culture-and-analysis satellite. in Microfluidics, BioMEMS, and Medical Microsystems IX vol. 7929 217–225 (SPIE, 2011).
61. Ehrenfreund, P. *et al.* The O/OREOS mission—Astrobiology in low Earth orbit. *Acta Astronaut.* 93, 501–508 (2014).
62. Padgen, M. R. *et al. EcAMSat* spaceflight measurements of the role of σs in antibiotic resistance of stationary phase *Escherichia coli* in microgravity. *Life Sci. Space Res.* 24, 18–24 (2020).
63. Padgen, M. R. *et al.* BioSentinel: A Biofluidic Nanosatellite Monitoring Microbial Growth and Activity in Deep Space. *Astrobiology* 23, 637–647 (2023).
64. Śniadek, P. *et al.* Autonomous, miniature research station (lab-payload) for the nanosatellite biological mission: LabSat. *Sci. Rep.* 15, 30898 (2025).
65. Lingam, N. *et al.* NASA’s BioSentinel deep space CubeSat mission: successes and lessons learned. *Acta Astronaut.* 236, 188–193 (2025).
66. Case, N., Johnston, N. & Nadeau, J. Fluorescence Microscopy with Deep UV, Near UV, and Visible Excitation for In Situ Detection of Microorganisms. *Astrobiology* 24, 300–317 (2024).
67. Schaefer, P. M., Kalinina, S., Rueck, A., von Arnim, C. A. F. & von Einem, B. NADH Autofluorescence—A Marker on its Way to Boost Bioenergetic Research. *Cytometry A* 95, 34–46 (2019).
68. De Ruyck, J. *et al.* Towards the understanding of the absorption spectra of NAD(P)H/NAD(P) + as a common indicator of dehydrogenase enzymatic activity. *Chem. Phys. Lett.* 450, 119–122 (2007).

69. Dougherty, M. et al. Results of the Micro-12 Flight Experiment: Effects of Microgravity on Shewanella oneidensis MR-1. (2019).
70. Bellary, R. et al. Voltage, power, and energy production of a Shewanella oneidensis biofilm microbial fuel cell in microgravity. J. Emerg. Investig. https://doi.org/10.59720/23-076 (2024) doi:10.59720/23-076.
71. Li, Y. C. *et al.* An Easily Fabricated Low-Cost Potentiostat Coupled with User-Friendly Software for Introducing Students to Electrochemical Reactions and Electroanalytical Techniques. *J. Chem. Educ.* 95, 1658–1661 (2018).
72. Rowe, A. R., Chellamuthu, P., Lam, B., Okamoto, A. & Nealson, K. H. Marine sediments microbes capable of electrode oxidation as a surrogate for lithotrophic insoluble substrate metabolism. *Front. Microbiol.* 6, 1–15 (2015).
73. Jangir, Y. *et al.* Isolation and Characterization of Electrochemically Active Subsurface Delftia and Azonexus Species. *Front. Microbiol.* 7, (2016).
74. Jangir, Y. *et al.* In situ Electrochemical Studies of the Terrestrial Deep Subsurface Biosphere at the Sanford Underground Research Facility, South Dakota, USA. *Front. Energy Res.* 7, (2019).
75. Harnisch, F., Deutzmann, J. S., Boto, S. T. & Rosenbaum, M. A. Microbial electrosynthesis: opportunities for microbial pure cultures. *Trends Biotechnol.* 42, 1035–1047 (2024).
76. Abboud, R. *et al.* Low-Temperature Growth of Shewanella oneidensis MR-1. *Appl. Environ. Microbiol.* 71, 811–816 (2005).
77. Araiza-Villanueva, M. G., Olicón-Hernández, D. R., Pardo, J. P., Vázquez-Meza, H. & Guerra-Sánchez, G. Monitoring of the enzymatic activity of intracellular lipases of < em>Ustilago maydis expressed during the growth under nitrogen limitation and its correlation in lipolytic reactions. *Grasas Aceites* 70, e327–e327 (2019).
78. Li, Y. *et al.* A chip-based scientific payload technology for visual detection of proteins and its application in spaceflight. *Acta Astronaut.* 170, 601–608 (2020).
79. Martirosyan, A. *et al.* Tracing transport of protein aggregates in microgravity versus unit gravity crystallization. *Npj Microgravity* 8, 4 (2022).
80. Ameur, Z. O. & Husein, M. M. Electrochemical Behavior of Potassium Ferricyanide in Aqueous and (w/o) Microemulsion Systems in the Presence of Dispersed Nickel Nanoparticles. *Sep. Sci. Technol.* 48, 681–689 (2013).
81. Department of Physics, Karnatak University Dharwad, India-580003, Mundinamani, S. P. & Rabinal, M. K. Cyclic Voltammetric Studies on the Role of Electrode, Electrode Surface Modification and Electrolyte Solution of an Electrochemical Cell. *IOSR J. Appl. Chem.* 7, 45–52 (2014).
82. Elgrishi, N. et al. A Practical Beginner's Guide to Cyclic Voltammetry. J. Chem. Educ. acs.jchemed.7b00361 (2017) doi:10.1021/acs.jchemed.7b00361.
83. Harnisch, F. & Freguia, S. A basic tutorial on cyclic voltammetry for the investigation of electroactive microbial biofilms. *Chem. - Asian J.* 7, 466–475 (2012).

84. Milojevic, T. & Weckwerth, W. Molecular Mechanisms of Microbial Survivability in Outer Space: A Systems Biology Approach. *Front. Microbiol.* 11, (2020).
85. Lang, J. M. *et al.* A microbial survey of the International Space Station (ISS). *PeerJ* 5, e4029 (2017).
86. Venkateswaran, K., La Duc, M. T. & Horneck, G. Microbial Existence in Controlled Habitats and Their Resistance to Space Conditions. *Microbes Environ.* 29, 243–249 (2014).
87. Pierson, D. L. et al. Microbial Monitoring of the International Space Station. in (Osaka, 2013).
88. Castro, V. A., Thrasher, A. N., Healy, M., Ott, C. M. & Pierson, D. L. Microbial Characterization during the Early Habitation of the International Space Station. *Microb. Ecol.* 47, 119–126 (2004).
89. Parra, M. *et al.* Microgravity validation of a novel system for RNA isolation and multiplex quantitative real time PCR analysis of gene expression on the International Space Station. *PLOS ONE* 12, e0183480 (2017).
90. Montague, T. G. *et al.* Gene expression studies using a miniaturized thermal cycler system on board the International Space Station. *PLOS ONE* 13, e0205852 (2018).
91. Kim, S., Park, S. & Pak, J. J. Multi-Modal Multi-Array Electrochemical and Optical Sensor Suite for a Biological CubeSat Payload. *Sensors* 24, (2024).

Figures

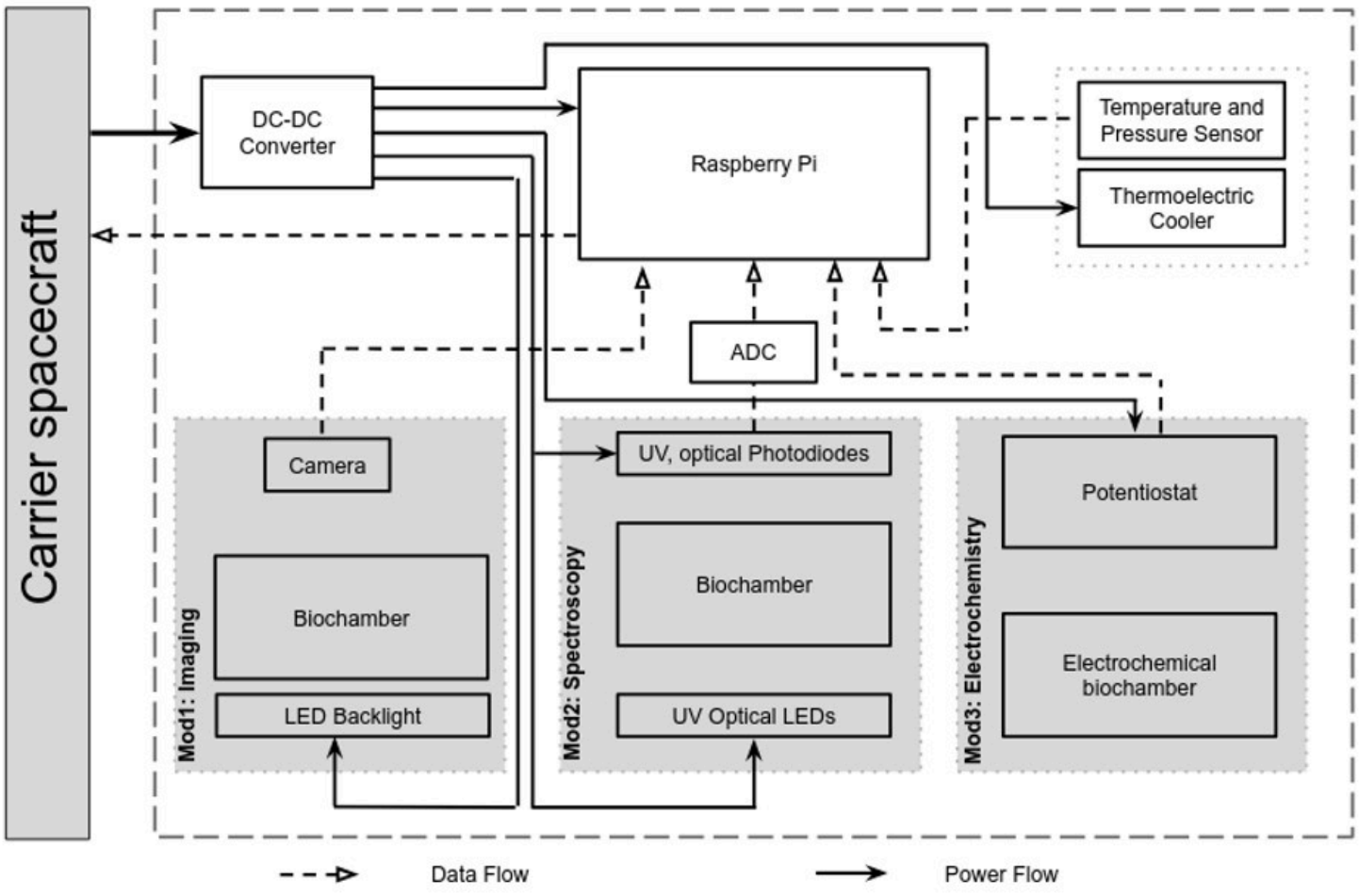


Figure 1

Power and signal flow diagram. Individual components are represented in blocks. The grey blocks with dotted lines as boundaries are three different analytical modules. The power flow is indicated with the solid arrows which flow to each component from the DC-DC converter which takes power from the carrier platform. The dashed arrows show the signal/data path which flows to RPi from every experiment and sensor and gets stored in the RPi. In a suitable time interval the stored data is transferred to the carrier platform to be relayed to the ground station.

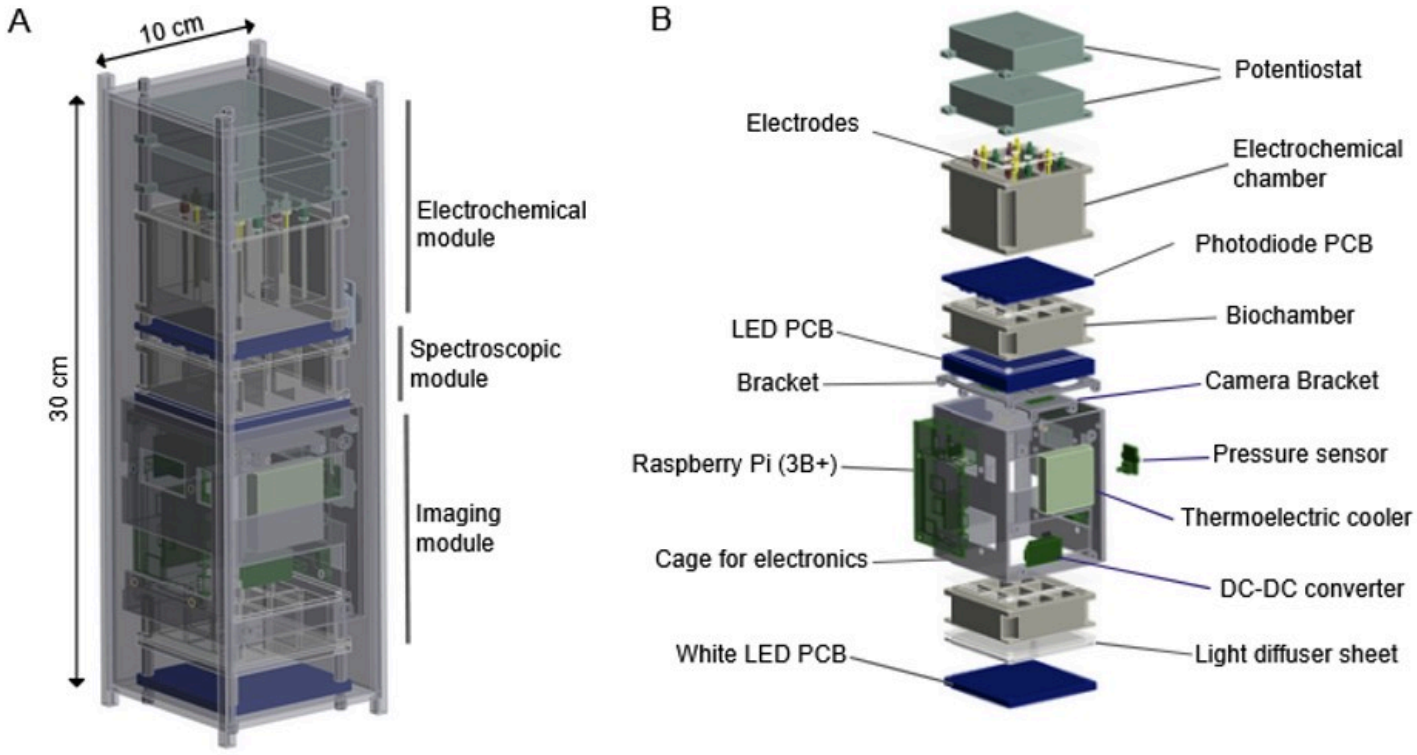


Figure 2

Structural overview of the Modular Astrobiology Experiment (MAEx) payload and integrated analytical modules. (A) Fully assembled MAEx payload showing the vertically integrated imaging, spectroscopic, and electrochemical modules within a 3U CubeSat-compatible architecture (10 × 10 × 30 cm). (B) Exploded view of the payload architecture illustrating modular subsystem integration (outer casing not shown). Electronic components and control systems are highlighted in green, custom LED and photodiode printed circuit boards (PCBs) are shown in blue, biochambers and electrochemical chambers are shown in grey, and the structural electronics cage and supporting framework are rendered in metallic silver-grey tones. The figure additionally highlights integration of the Raspberry Pi controller, potentiostat modules, thermoelectric cooling system, pressure sensor, illumination system, and imaging assembly within the payload structure.

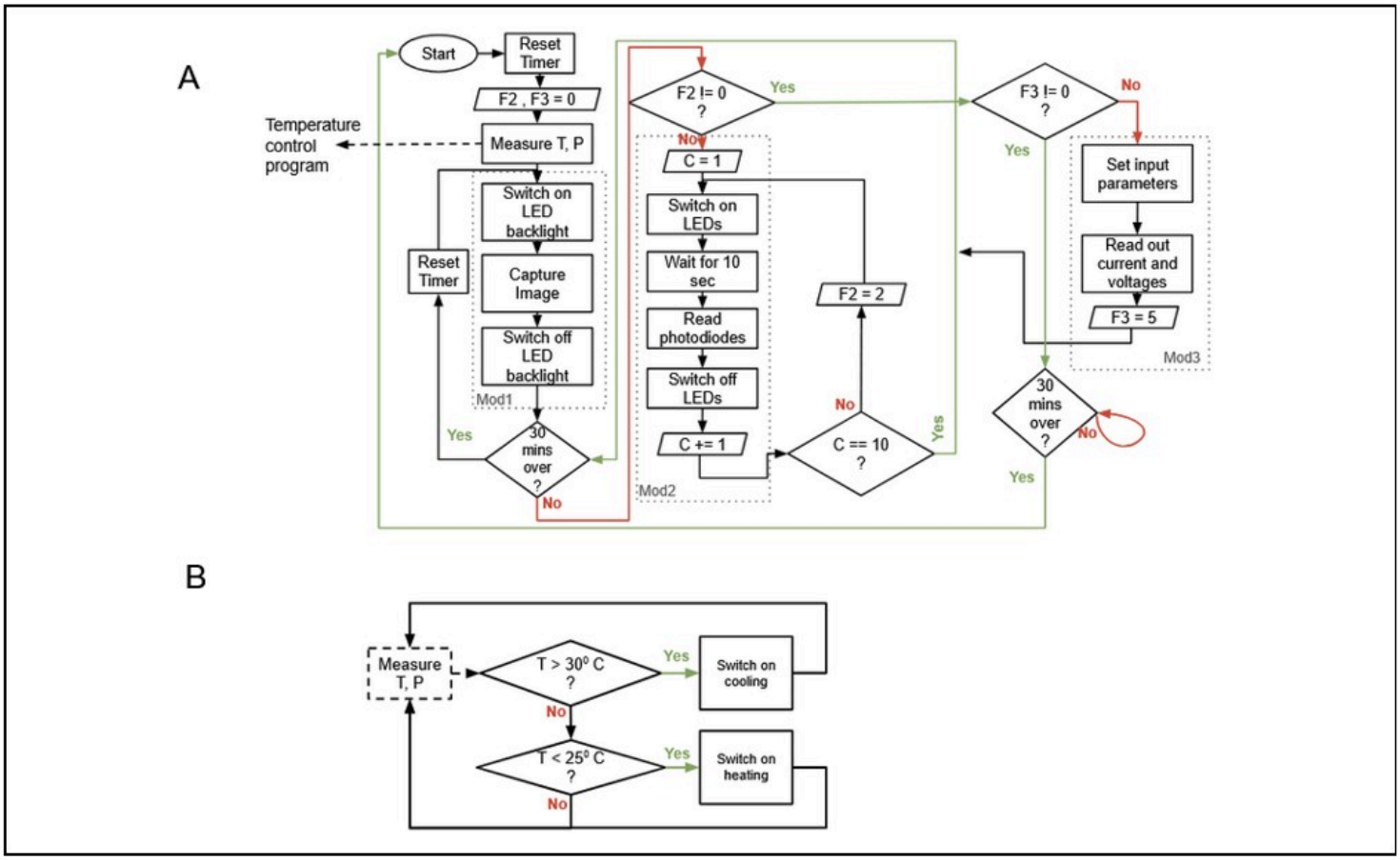


Figure 3

(A) Flowchart illustrating the sequential execution of experiments controlled by the Raspberry Pi (RPi), including the imaging module (Mod1), spectroscopic module (Mod2), and electrochemical module (Mod3). F2 and F3 represent flag variables indicating whether the spectroscopic and electrochemical experiments, respectively, were executed during a given iteration. Conditional timing blocks for 30 min intervals were implemented using a universal timer that was reset after each acquisition cycle. (B) Flowchart of the independent temperature-control program used to regulate and maintain payload temperature during operation.

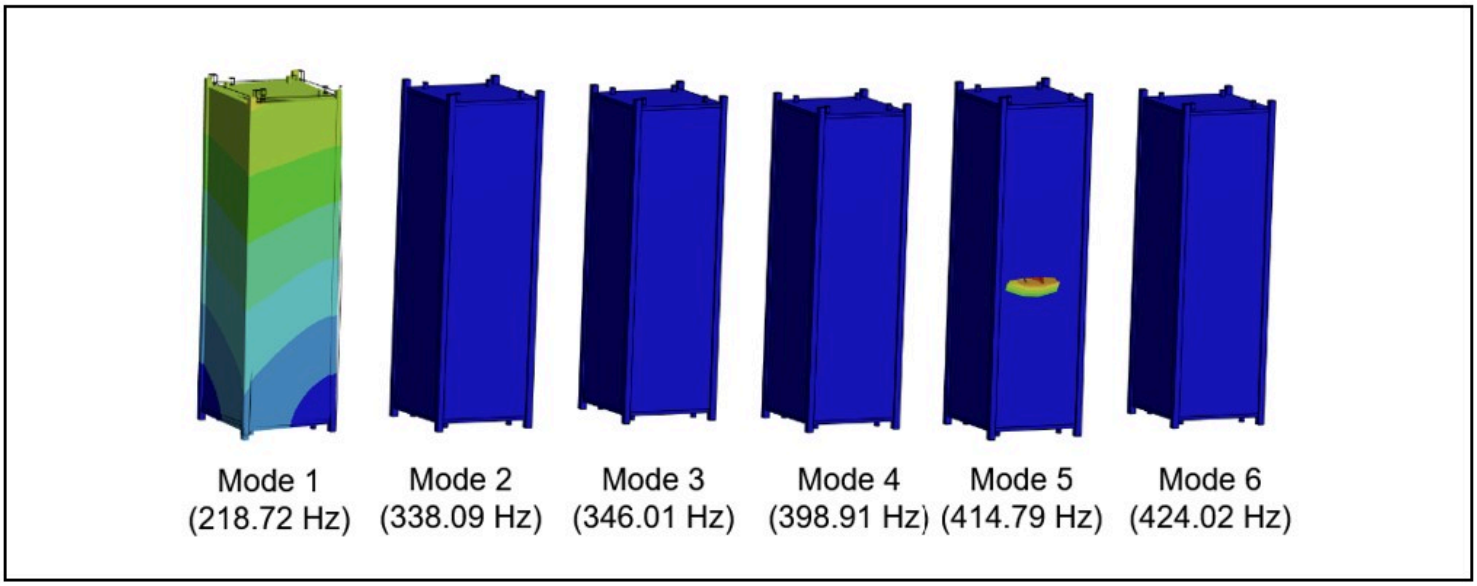


Figure 4

Finite element modal simulations were performed to evaluate the dynamic structural response of the MAEx payload under launch-relevant conditions. The first six vibration modes and their corresponding natural frequencies are shown. The dominant structural mode (Mode 1) was identified at 218.72 Hz based on the highest effective mass and participation factor values. Since this frequency is substantially higher than the expected natural frequency range of the host spacecraft (70-90 Hz), the MAEx payload is expected to remain outside the resonance regime during nominal launch conditions. Forced vibrational analysis is still pending.

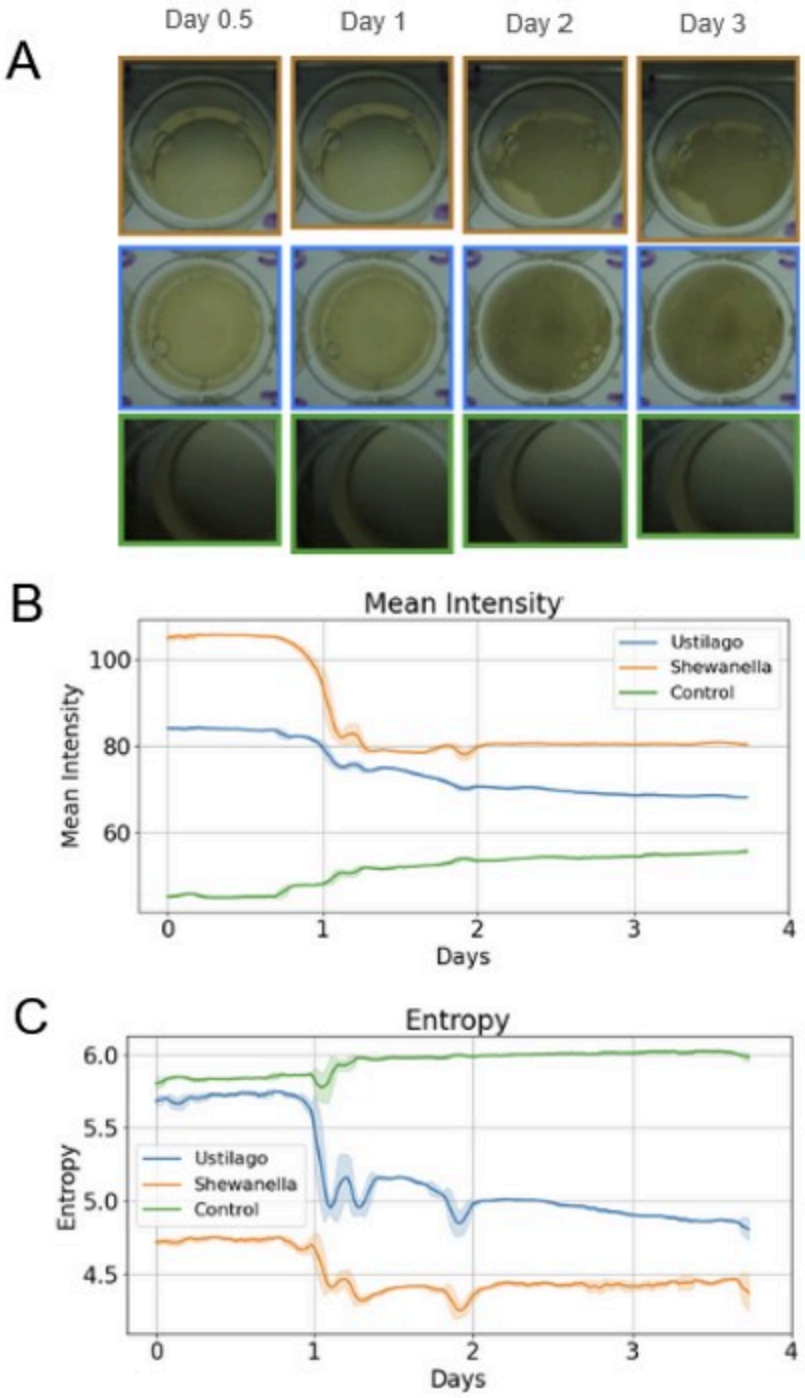


Figure 5

(A) Representative snapshots of microbial growth acquired using the Raspberry Pi imaging module at different experimental timepoints. Embedded timestamps indicate the corresponding acquisition time during payload operation. (B) Quantitative image analysis of microbial growth based on temporal changes in mean image intensity. Mean intensity values were normalized to the maximum mean intensity observed across the experimental time series to enable comparative analysis of growth dynamics over time.

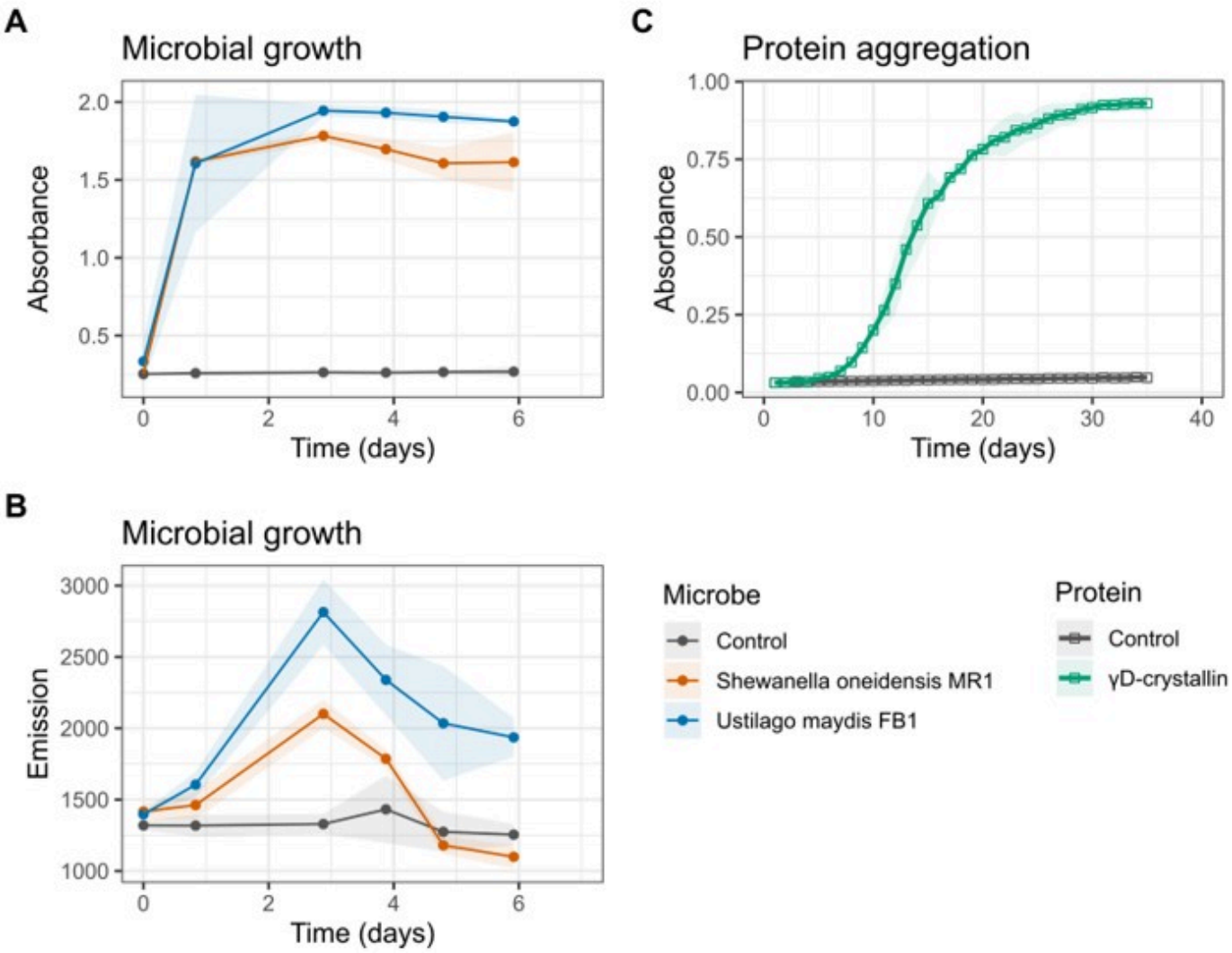


Figure 6

(A) Optical density (OD_{600}) and (B) fluorescence intensity (Ex/Em: 340/480 nm) measured during growth of *S. oneidensis* MR1 and *U. maydis* FB1 in YPD agar-based medium at 25°C. (C) Optical density (OD_{365}) measured during γD-crystallin aggregation at 25°C.

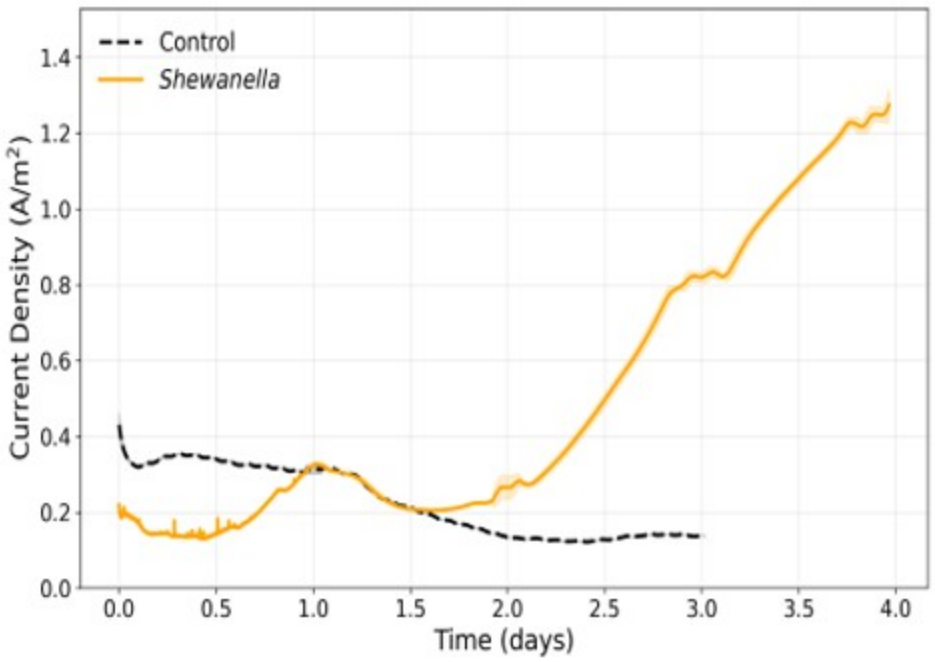


Figure 7

Anodic current production by *S. oneidensis* MR1 in 5 g-sediment slurry under oxic conditions at 1 atm pressure at 25°C.

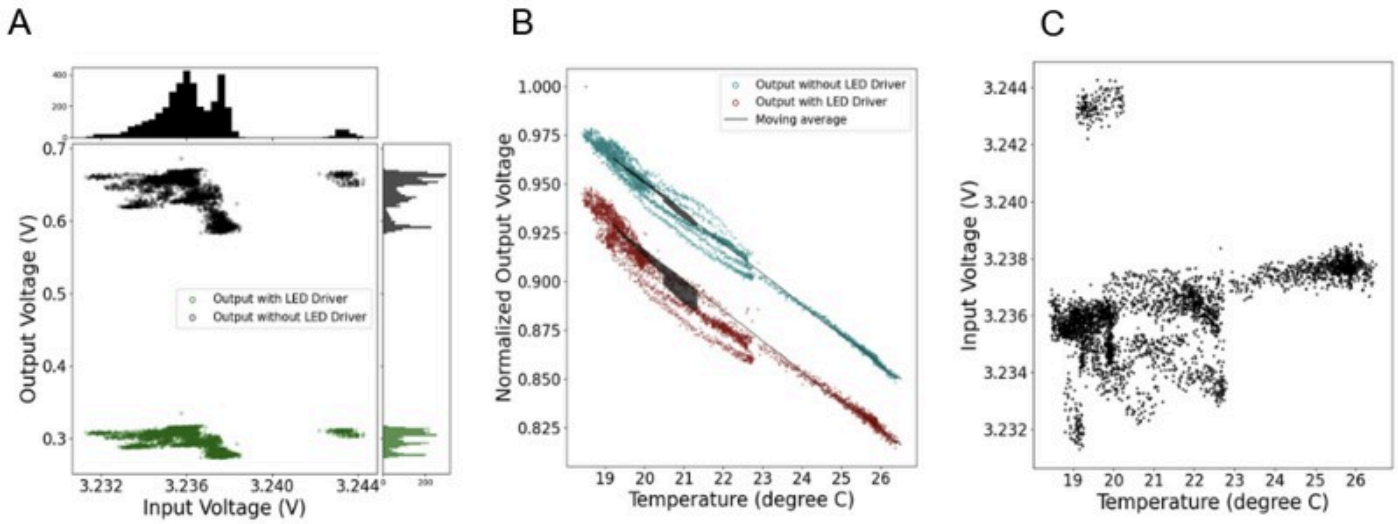


Figure 8

(A) Distribution of red LED input voltage (from GPIO pin of Raspberry Pi) and output voltage from OPT101P and their interdependence under two conditions (black : when LED is connected directly, green : when LED is connected through LED driver); (B) Dependance of the output voltages with temperature; (C) dependance of LED input voltage (GPIO pin of Raspberry Pi) with temperature

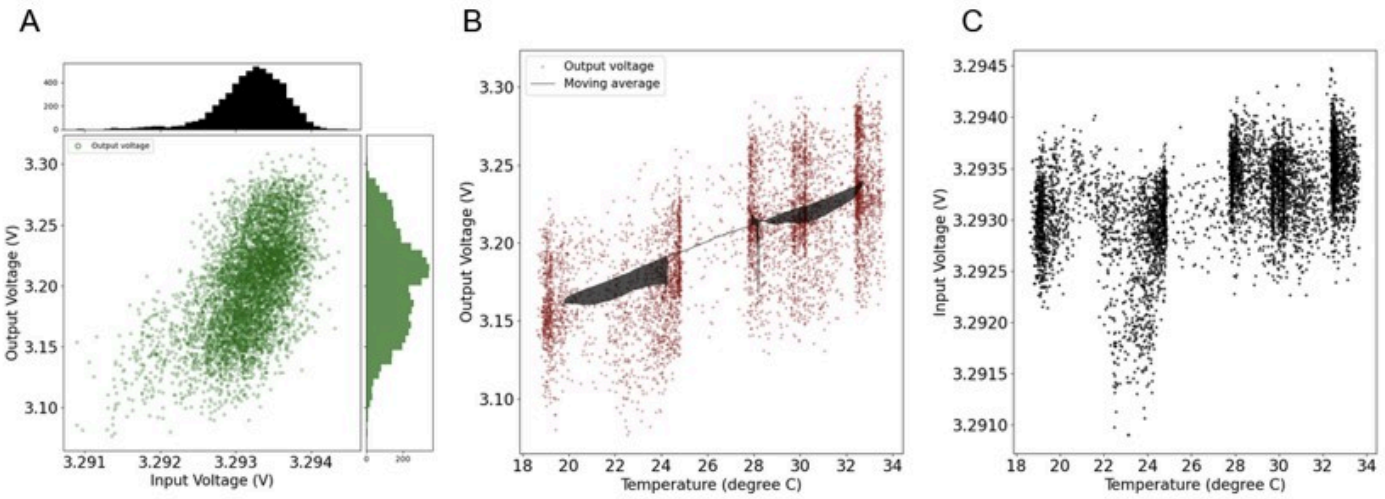


Figure 9

(a) Distribution of LED input voltage (from GPIO pin of Raspberry Pi) and output voltage from UV photodiode and their interdependence; (b) Dependance of the output voltages with temperature; (c) dependance of LED input voltage (GPIO pin of Raspberry Pi) with temperature.

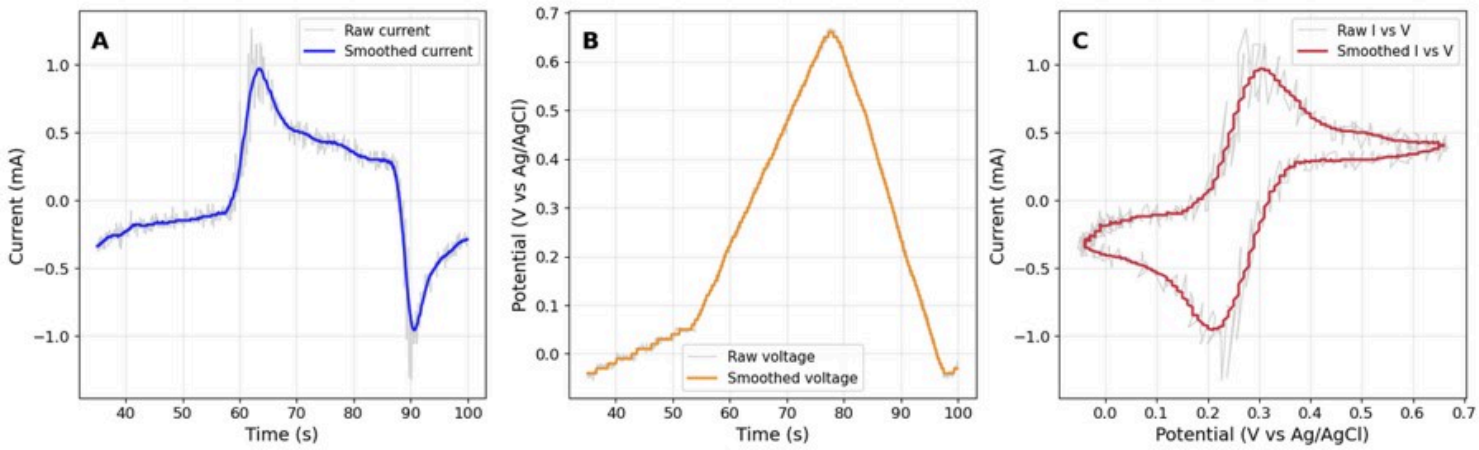


Figure 10

Electrochemical characterization of the MAEx potentiostat module. Cyclic voltammetry measurements were performed using 5 mM $K_3Fe(CN)_6$ dissolved in 0.1 M KNO_3 electrolyte to validate the electrochemical performance of the MAEx potentiostat system. (A) Time-resolved current response, (B) applied potential profile versus Ag/AgCl reference electrode, and (C) corresponding current–potential (I–V) voltammogram. Grey traces represent raw measurements, while colored traces indicate smoothed profiles. The voltammograms exhibit characteristic oxidation and reduction peaks associated with the $Fe(CN)_6^{3-}/Fe(CN)_6^{4-}$ redox couple, with the midpoint potential of ca. 0.28 V.

Supplementary Files

This is a list of supplementary files associated with this preprint. Click to download.

- SupplementaryMaterial.docx